



The Massive and Distant Clusters of WISE Survey. X. Initial Results from a Sunyaev–Zeldovich Effect Study of Massive Galaxy Clusters at $z > 1$ Using MUSTANG2 on the GBT

Simon R. Dicker¹, Charles E. Romero^{1,2}, Luca Di Mascolo³, Tony Mroczkowski⁴, Jonathan Sievers⁵, Emily Moravec⁶, Tanay Bhandarkar¹, Mark Brodwin⁷, Thomas Connor⁸, Bandon Decker⁷, Mark Devlin¹, Anthony H. Gonzalez⁹, Ian Lowe¹, Brian S. Mason¹⁰, Craig Sarazin¹¹, Spencer A. Stanford¹², Daniel Stern⁸, Khunanon Thongkham⁹, Dominika Wylezalek⁴, and Fernando Zago⁵

¹ Department of Physics and Astronomy, University of Pennsylvania, 209 South 33rd Street, Philadelphia, PA 19104, USA; sdicker@hep.upenn.edu

² Green Bank Observatory, Green Bank, WV 24944, USA

³ Max-Planck-Institut für Astrophysik (MPA), Karl-Schwarzschild-Strasse 1, Garching D-85741, Germany

⁴ ESO—European Southern Observatory, Karl-Schwarzschild-Strasse 2, D-85748 Garching b. München, Germany

⁵ Department of Physics, McGill University, 3600 University Street Montreal, QC H3A 2T8, Canada

⁶ Astronomical Institute of the Czech Academy of Sciences, Boční II 1401/1A, 14000 Praha 4, Czech Republic

⁷ Department of Physics and Astronomy, University of Missouri, 5110 Rockhill Road, Kansas City, MO 64110, USA

⁸ Jet Propulsion Laboratory, California Institute of Technology, 4800 Oak Grove Drive, Pasadena, CA 91109, USA

⁹ Department of Astronomy, University of Florida, 211 Bryant Space Center, Gainesville, FL 32611, USA

¹⁰ National Radio Astronomy Observatory, 520 Edgemont Road, Charlottesville VA 22903, USA

¹¹ Department of Astronomy, University of Virginia, P.O. Box 400325, Charlottesville, VA 22901, USA

¹² Department of Physics, University of California, One Shields Avenue, Davis, CA 95616, USA

Received 2020 June 5; revised 2020 August 31; accepted 2020 September 7; published 2020 October 23

Abstract

The properties of galaxy clusters as a function of redshift can be utilized as an important cosmological tool. We present initial results from a program of follow-up observations of the Sunyaev–Zeldovich effect (SZE) in high-redshift galaxy clusters detected by the Massive and Distant Clusters of WISE Survey (MaDCoWS) which uses infrared data from the Wide-field Infrared Survey (WISE) instrument. Using typical on-source integration times of 3–4 hr per cluster, MUSTANG2 on the Green Bank Telescope was able to measure strong detections of SZE decrements and statistically significant masses on 14 out of 16 targets. On the remaining two, weaker (3.7σ) detections of the SZE signal and strong upper limits on the masses were obtained. In this paper we present masses and pressure profiles of each target and outline the data analysis used to recover these quantities. Of the clusters with strong detections, three show significantly flatter pressure profiles while, from the MUSTANG2 data, five others show signs of disruption at their cores. However, outside of the cores of the clusters, we were unable to detect significant amounts of asymmetry. Finally, there are indications that the relationship between optical richness used by MaDCoWS and SZE-inferred mass may be significantly flatter than indicated in previous studies.

Unified Astronomy Thesaurus concepts: [Sunyaev-Zeldovich effect \(1654\)](#); [High-redshift galaxy clusters \(2007\)](#)

1. Introduction

The study of clusters of galaxies is important to our understanding of the universe. For example, the mass of clusters as a function of redshift helps us understand the formation of structure and constrains cosmological parameters such as σ_8 (Allen et al. 2011). By looking at the internal dynamics of clusters one can obtain insight to processes such as the interaction between active galaxies and the intracluster medium (ICM) where most of the baryons of a cluster reside. With merging clusters one is able to make inferences as to the nature of dark matter. To utilize clusters as a tool in this way, extensive catalogs of galaxy clusters are needed. Of particular value are catalogs with well known selection functions that include massive objects at high redshifts. Early catalogs were made by measuring the overdensity of galaxies observed at optical wavelengths (Abell 1958). At low redshift, massive clusters are also easily identified by the strong X-ray emission from the hot gas in the ICM. All-sky surveys from instruments such as ROSAT have made extensive catalogs (e.g., Cruddace et al. 2002). At higher redshifts cosmic dimming becomes significant and even the most massive clusters have low X-ray surface brightness. Above $z \gtrsim 1$ clusters are expected to be

hotter and denser and surface brightness should not decrease further (e.g., Churazov et al. 2015), but these clusters will still have low X-ray surface brightness. Thus, long integration times are required and X-ray surveys are limited to small areas ($<100 \text{ deg}^2$; e.g., Fassbender et al. 2011). As a result current X-ray surveys do not probe the volume required to meaningfully sample the high-mass end ($M > 5 \times 10^{14} M_\odot$) of the high-redshift cluster mass function. There are alternative methods of searching for clusters such as using the Sunyaev–Zeldovich effect (SZE) that do not suffer from cosmological dimming (for a review, see Carlstrom et al. 2002). However, current surveys from the SPT (Williamson et al. 2011; Bleem et al. 2015, 2020; Huang et al. 2020) and ACT (Marriage et al. 2011; Hasselfield et al. 2013; Hilton et al. 2018) still only cover a few thousand square degrees. All-sky SZE surveys from experiments such as Planck (Planck Collaboration et al. 2015) are limited to low redshift clusters due to large beam sizes.

Clusters at redshifts $z > 1$ provide far greater leverage on cosmological parameters—for example, the discovery of even a few massive clusters at high enough redshifts could rule out some cosmological models (Holz & Perlmutter 2012). Also the current relationships between cluster mass and cluster properties are based on extrapolations from low to moderate redshifts.

Table 1
A Summary of Our MUSTANG2 Observations

Cluster ID ^a	R.A. (J2000)	Decl. ^b	Redshift ^c	Time On Src (hr) ^d	Map Noise ^e ($\mu\text{K}_{\text{Main beam}}$)	Peak S/N per 10'' beam	Overall Detection	Jy to K (K Jy^{-1}) ^f
MOO 0105	01:05:30.45	+13:24:01.9	1.143 s	2.0	42	-7.3	8.0σ	1.43
MOO 0135	01:35:04.31	+32:07:27.2	1.46	4.9	29	-4.6	5.9σ	1.46
MOO 1014	10:14:07.49	+00:38:30.2	1.230 s	2.7	23	-11.1	29.3σ	1.49
MOO 1031	10:31:48.23	+62:55:30.5	1.33	3.4	45	-3.8	3.7σ	1.50
MOO 1046	10:46:52.82	+27:58:02.9	1.16	2.3	36*	-9.5	9.5σ	1.20
MOO 1052	10:52:15.30	+08:23:53.0	1.41	3.6	23*	-6.1	7.2σ	1.48
MOO 1054	10:54:56.00	+05:05:39.0	1.44	5.4	19*	-3.3	5.3σ	1.47
MOO 1059	10:59:50.83	+54:54:58.4	1.14	7.1	11	-7.5	53.1σ	1.33
MOO 1108	11:08:48.00	+32:43:35.8	1.12	6.7	14	-5.5	19.2σ	1.37
MOO 1110	11:10:57.15	+68:38:30.7	0.93	7.3	12	-8.0	15.5σ	1.44
MOO 1142	11:42:45.51	+15:27:15.4	1.189 s	5.2	13*	-14.5	20.9σ	1.40
MOO 1203	12:03:07.00	-09:09:13.0	1.24	4.6	23*	-4.5	3.7σ	1.43
MOO 1322	13:22:56.30	-02:28:15.0	0.82	2.7	28*	-8.1	9.5σ	1.39
MOO 1329	13:29:48.00	+56:47:39.0	1.43	1.5	46*	-7.8	19.2σ	1.59
MOO 1354	13:54:51.70	+13:29:36.0	1.48	3.8	13*	-9.2	9.4σ	1.58
MOO 1506	15:06:20.35	+51:36:53.6	1.09	5.7	36*	-6.5	11.3σ	1.38

Notes.

^a Full MaDCoWS cluster names are given in Table 3.

^b Coordinates are from the MaDCoWS survey (Gonzalez et al. 2019) and represent the center of the galaxy over density.

^c Redshifts from Gonzalez et al. (2019). Redshifts are photometric, except when marked with an “s,” in which case they are spectroscopic.

^d Data were taken over more than 20 separate nights. As MUSTANG2’s sensitivity is limited by the atmosphere, some nights have far greater weight than others. Totals only include data used in each map.

^e Map noise refers to the standard deviation at the center of the maps while the overall significance of the detections comes from the fitting of pressure profiles to the calibrated timestreams in Minkasi. A * indicates a four-pointing-centers observational strategy was used.

^f At 90 GHz, thermal effects cause the beam of the GBT to degrade over an observing session and the quality of the focus achievable each night varies at a 25% level. These values are weighted averages of the scans used for each source.

In order to find the high-redshift counterparts of the lower redshift clusters that dominate current cluster surveys, the Massive and Distant Cluster of WISE Survey (MaDCoWS) project was conceived. IR galaxies are selected from the Wide-field Infrared Survey Explorer (WISE) all-sky IR survey (Wright et al. 2010). Using color cuts and additional data from the Sloan Digital Sky survey, likely clusters were located by looking for peaks in the number density of high-redshift galaxies. A full description of the methods used and the clusters found in the 10,000 deg² searched can be found in Gonzalez et al. (2019). Follow-up observations have included SZE measurements using the Combined Array for Millimeter-wave Astronomy (CARMA) (Brodwin et al. 2015) and the Atacama Compact Array (ACA; also known as the Morita Array; Di Mascolo et al. 2020) in order to more easily compare masses obtained from richness to the mass scales used by SZE experiments. In this paper we present initial results of a follow-up program in the SZE using MUSTANG2 on the 100 m Green Bank Telescope (GBT), operated by the Green Bank Observatory. The cluster sample was chosen based on visibility from the GBT and so will contain the same selection biases (e.g., Malmquist bias at low richness) as MaDCoWS. The 16 clusters presented here were the first observed from this sample with a priority partly chosen due to scheduling constraints and the availability (or lack of) auxiliary data sets. As well as obtaining masses from the total integrated SZE signal (Y) these high resolution (10'') measurements of the SZE allow one to measure the cluster profiles, identify and remove point sources, and classify cluster dynamical states (see Mroczkowski et al. 2019, for a review of the application of high resolution studies of the SZE).

The paper is organized as follows. In Section 2 we outline our observations and in Sections 3 and 4 we provide an overview of the data reduction pipelines and the tests used to confirm our ability to recover masses and pressure profiles. Our results, including recovered pressure profiles, masses, comparisons of our SZE masses with optical richness, and notes on the symmetry of the clusters, are presented in Sections 5–7. Our conclusions are in Section 8. Throughout this paper we assume a Λ CDM concordance cosmology with $H_0 = 70 \text{ km s}^{-1} \text{ Mpc}^{-1}$, $\Omega_M = 0.3$, and $\Omega_\Lambda = 0.7$.

2. Observations

From 2018 October to 2020 February, a total of 95 hr (69 hr excluding setup and calibration) were spent observing clusters from the MaDCoWS sample using the MUSTANG2 bolometer camera (Dicker et al. 2014) on the GBT. MUSTANG2 has a bandpass of 75–105 GHz and a resolution of $\sim 10''$. A summary of the on-source integration time, the noise level, signal-to-noise ratio (S/N), and detection significance for each cluster observed is given in Table 1. Observations were carried out using a daisy scanning pattern (shown in Figure 1) designed to cross the cluster on timescales faster than expected atmospheric noise (10 s), to provide many redundant observations, and to ensure all detectors get off-source. Scan radii of 2.5' and 3' were used that, when the detector array’s field of view (FoV) is taken into account, provided good coverage over the $\sim 7'$ diameter of the maps. Each daisy scanning pattern, referred to as a scan, takes 500 s to complete. During early data analysis (Section 3), it was found that, under some circumstances, incomplete removal of common mode atmospheric emission from the time ordered data of each scan (timestreams) could leave structure in the elevation direction. When combined with

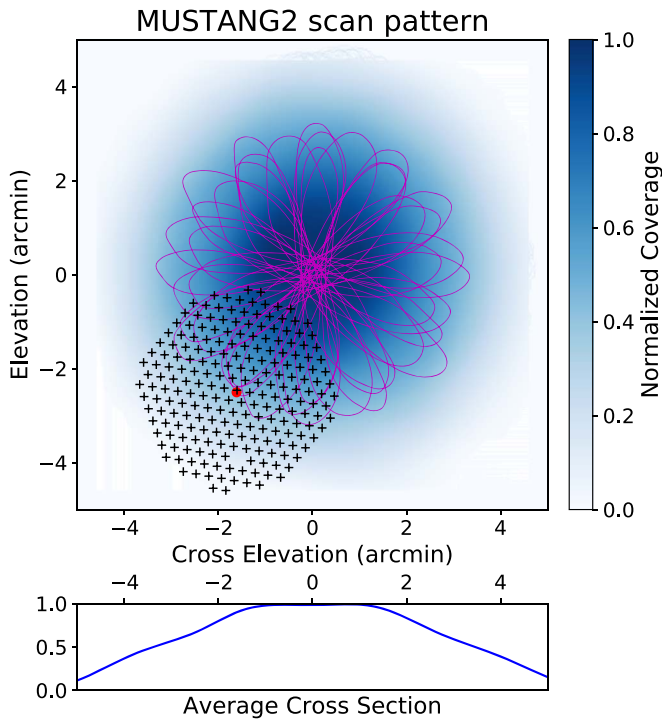


Figure 1. The scan pattern used on these clusters superimposed on the normalized depth of the coverage. The magenta lines represent the path of the central detector of the array. Shown in the bottom left is the footprint of the array with the central detector marked as the red dot. The scan pattern is designed to provide cross-linking on many different timescales, between all parts of the array. The scan period (10 s) is set as short as possible within the limits of the GBT’s servo system so as to reduce the effects of $1/f$ noise from the atmosphere and receiver. In later observations, four different pointing centers at $\pm 1.5'$ were used for each cluster. This enabled more robust removal of residual atmospheric noise (Section 2). The bottom plot shows a cross-section through the center of the normalized depth.

sky rotation, this resulted in cluster-sized noise features in the maps. To reduce these features, instead of a single pointing center at the location of the MaDCoWS cluster location, later data were collected with four centers, offset from the MaDCoWS center by $\pm 1.5'$ in R.A. or decl.

Approximately every 20 minutes a nearby bright point source was observed. This was used to check the focus in real time and later on, during data reduction, to calibrate the raw detector timestreams. Most of these secondary calibrators were quasars with unknown, possibly variable, flux at 90 GHz so at least once a night their flux was tied to an absolute calibrator. When available, we made use of the planet Uranus while at other times we used flux calibrators commonly used by the Atacama Large Millimeter/submillimeter Array (ALMA). These flux calibrators are regularly monitored by ALMA at 100 and 91 GHz¹³ and their flux was extrapolated in both time between ALMA observations and in frequency (to account for the difference in ALMA’s and MUSTANG2’s bandpasses). The flux of the secondary calibrators (in Jy) was assumed to be constant over each night.

3. Data Reduction

This paper makes use of two different data reduction pipelines, MIDAS and Minkasi. MIDAS is based on MUSTANG-1’s IDL pipeline (Mason et al. 2010; Korngut et al. 2011;

Romero et al. 2015; Young et al. 2015). Minkasi is a maximum likelihood pipeline based on the one used by the ACT collaboration (Dünner et al. 2013). Although both pipelines can produce maps, fit point sources, and find cluster surface brightness profiles, in this paper we only present maps made by MIDAS and profiles and point-source fits using Minkasi. Calibration of raw MUSTANG2 data for both pipelines is carried out using the following steps in MIDAS:

1. An initial flat-fielding of the array is made using a skydip taken at the beginning of each night’s observations. Unresponsive detectors are flagged and their data discarded.
2. At this stage most of the signal in the timestreams is atmospheric emission and should be the same in all detectors. To account for relative gain drifts between detectors, the timestreams are renormalized such that the first principle component has the same amplitude in each detector.
3. Maps of all calibrator sources are made and fits to the peak height and beam volume carried out. A calibration factor to Jy is obtained by taking the ratio of the expected peak to the measured one. Additionally, a calibration to (main beam) brightness temperature is calculated by using the fitted beam volume. The atmospheric opacity is obtained using archival weather data via the GBT’s observing tools—this is then used to adjust for any differences in elevation between calibrators and our clusters.
4. The calibration factors from step 3 are extrapolated between observations of the secondary calibrators and are applied to the cluster scans to produce calibrated timestreams.
5. A number of heuristics are used to detect glitches (such as jumps caused by readout errors) in individual detector timestreams. For small glitches, only part of a timestream is masked out while timestreams showing many glitches or excess noise are dropped completely.

The resulting timestreams from this process are passed on to the map making stage of MIDAS (described next) or saved to a disk for later use by Minkasi. Overall, we estimate there is a 10% error in our absolute calibration of the observations presented in this paper. Sources of this error include the fits to the primary and secondary calibrators, the assumed flux of the absolute calibrator in our band, and our knowledge of the atmospheric opacity.

3.1. MIDAS Map Making

In addition to calibrating the timestreams, MIDAS was used to make the maps presented in this paper. In the calibrated detector timestreams the cluster’s signal can easily be a factor of 10^5 below atmospheric emission and $1/f$ noise from the detectors. However, our scanning pattern means that point sources pass through the beam at ~ 10 Hz, while the entire map is crossed once every 10 s, so frequencies $f \gg 10$ Hz and $f \ll 0.1$ Hz contain very little astronomical signal and can be filtered out. This still leaves a significant noise due to the change in optical depth as the GBT scans in elevation. However, this noise, along with contributions to the noise from the readout electronics, are all highly correlated. Using a principle component analysis it is possible to subtract these contributions before binning the data into a map. In the 16

¹³ <https://almascience.eso.org/alma-data/calibrator-catalog>

cluster maps presented in this paper, filter bandpasses of 0.065–41 Hz were used and the first three principle components were subtracted before map making.

Because of the Fourier filter, MIDAS maps are not unbiased. Features on the largest angular scales can have Fourier components below 0.065 Hz and will be slightly attenuated. Features of the order of the map size or greater are mostly DC and are thus not detected at all. To quantify this we create fake MUSTANG2 data using real timestreams reversed in time to smear out any astronomical signals. A fake sky containing random structure on all angular scales is sampled then added to the reversed timestreams and the results passed through the MIDAS pipeline to obtain a recovered sky map. A transfer function can be defined by the ratio between the FFTs of the fake and recovered sky maps averaged over many versions of the noise and sky. Tests with the data reduction parameters used in this paper show that we recover all angular scales up to 5' (diameter) although at angular scales larger than R_{500} ($\sim 3'$ diameter for typical MaDCoWS clusters) small corrections are needed. To circumvent this problem, in this paper we choose to present cluster profiles made using the Minkasi pipeline discussed next.

3.2. Minkasi and Brightness Profiles

As described in Romero et al. (2020), surface brightness profiles can be calculated by Minkasi. Minkasi operates on the calibrated but unfiltered timestreams output by MIDAS. It simultaneously fits multiple parameters directly to timestreams—for example, the location, width, and amplitudes of point sources, without going through map space. A full covariance matrix is recovered and the results are unbiased by Fourier filtering—to the extent that the signal is present in the raw data, no transfer function needs to be considered.

Fitting the brightness profiles to clusters is a two step process. First, the centers of the cluster and any point sources detected at greater than 4σ in the MIDAS maps are found using a weighted least squares fit to all data on each cluster. Symmetrical Gaussian shapes are assumed. Weights for each detector in each scan are derived using a singular value decomposition (SVD) technique. The timestreams are rotated into SVD space, a power spectrum is taken, and the results are smoothed in order to obtain a better estimate of the true underlying power spectrum. Alternatives to smoothing would be the averaging of power spectra from different scans but the noise in MUSTANG2 data can vary significantly and this was found to give incorrect weights. Once smoothed power spectra in SVD space are obtained, they are rotated back into timestream space and used in a weighted least squares fit for the cluster's (and any point sources') amplitude, width, and location. This is done iteratively so that the astronomical signal does not bias the noise estimate. In each iteration, the results from the previous iteration are subtracted from the timestreams before recalculation of the noise and then added back in. Tests showed convergence in as few as five iterations; however, we used a conservative 15 iterations.

With the centers fixed, this process is repeated with parameters of the amplitude of each point source (if any) and the surface brightness in fixed annuli around the cluster center found in the last step. Our initial results (Section 5) assumed circular symmetry but later azimuthally segmented annuli were used (Section 7).

3.3. Pressure Profiles

Of more intrinsic interest than surface brightness profiles in understanding the physics of clusters are cluster masses and shapes of the pressure profiles. Using the method described in greater detail in Romero et al. (2020), it is possible to deproject the brightness profiles and obtain pressure profiles. A fit to the brightness profile assuming a nonparametric model of the cluster with six shells spaced logarithmically in radius between $10''$ and $200''$ is carried out. If either of the outer bins had a fitted pressure less than 2σ from zero, then the fit was repeated excluding these bins. Within each bin the pressure is assumed to follow a power law with the slope in the last bin constrained to go to zero at infinity. Assuming the redshifts from Gonzalez et al. (2019; reproduced in Table 1), adopting a temperature of 4–5 keV (appropriate for clusters in this mass range e.g., Bulbul et al. 2019), the relativistic corrections to the thermal SZE given in Itoh et al. (1998), and using the known MUSTANG2 beam shape (found in the initial calibration), these bins can be integrated analytically to obtain a brightness profile. Iterations using the Markov Chain Monte Carlo (MCMC) package `emcee` (Foreman-Mackey et al. 2013) make use of the covariance matrix from Minkasi to find the most likely pressure profile. From the nonparametric profile, a spherically integrated $Y(r)$ is calculated. Using the approach in Romero et al. (2020) a Y_{500} is self-consistently calculated assuming a Y – M relation derived from the universal pressure profile (Equation (22) in Arnaud et al. 2010, hereafter A10). Other Y – M relationships could have been used but, as Romero et al. (2020) show, in our mass range, differences between scaling relations are less than 20%. All these relationships have potential biases. In this work there is no strong astrophysical reason to prefer one Y – M relation over another so we chose the relation from A10 as it is well established, making comparisons with past work (e.g., Ge et al. 2019; Castagna & Andreon 2020) easier. The A10 pressure profiles shown in Figure 2 are thus the A10 pressure profiles for the M_{500} we derived from the Y – M relation. As stated in Romero et al. (2020), this process has been shown to be robust against initial assumptions on a cluster's shape, mass, and electron temperature.

One concern when using SZE measurements to measure masses is that point sources cancel out the SZE decrement, biasing masses low. Interferometers such as ACA, CARMA, or ALMA can constrain the flux contributions from such sources using their long baselines. Likewise, MUSTANG2's high resolution allows the easy removal of any source significantly above the noise floor in the maps (20–50 μK see Table 2). No attempt was made to fit sources detected at 4σ or less but these will have fluxes below 200 μK . In the central few bins of a cluster's pressure profile such sources can slightly lower the pressure (as sources will always be positive and the SZE signal is negative) but when averaged over the whole cluster (several arcminutes squared) their effect on our mass determinations was expected to be negligible. To confirm this assumption, fake sources that were not modeled when fitting the rings were added to our real timestreams and the data were reanalyzed using identical steps as those used to recover the masses in Table 3. Source amplitudes up to 400 μK ($>8\sigma$ depending on the cluster) were used and these changed recovered masses by less than 3%. The largest errors on our recovered fluxes are 260 μK so errors in the recovered cluster masses due to poor fits to point sources should also be negligible.

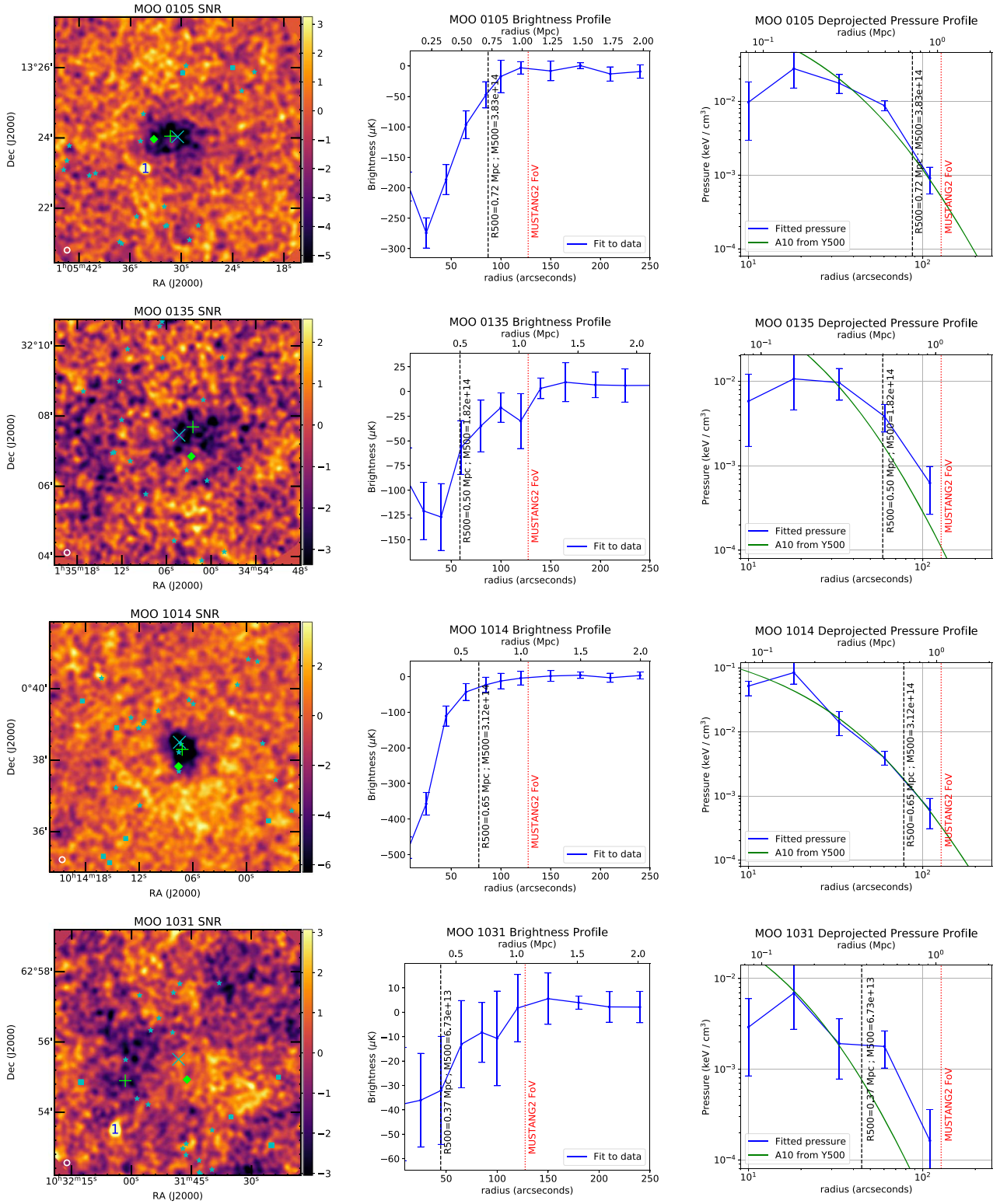


Figure 2. Left: MUSTANG-2 images made using the MIDAS pipeline. A cyan X marks the original center found by MaDCoWS, while the green cross marks the best-fit SZE centroids. Cyan stars and squares mark the locations of bright galaxies detected by Spitzer and SDSS, respectively. The BCG is marked as a green diamond and the MUSTANG2 beam is shown as a white circle on the lower left. The bright sources are clipped at $+4\sigma$ and are labeled with numbers to match Table 2. Center: brightness profiles of our clusters from Minkasi. Right: pressure profiles derived from each data set. The MUSTANG2 FoV is marked as a red line, while the black dashed line represents the R_{500} for our recovered mass. The A10 profile that corresponds to this mass is shown in green.

4. Simulations

In order to confirm our ability to recover masses and pressure profiles, we performed simulations of our observations and

analysis pipeline. Complete end-to-end tests were carried out by creating fake cluster profiles at known redshifts between 0.7 and 1.4 (to cover the range of redshifts in our sample) and

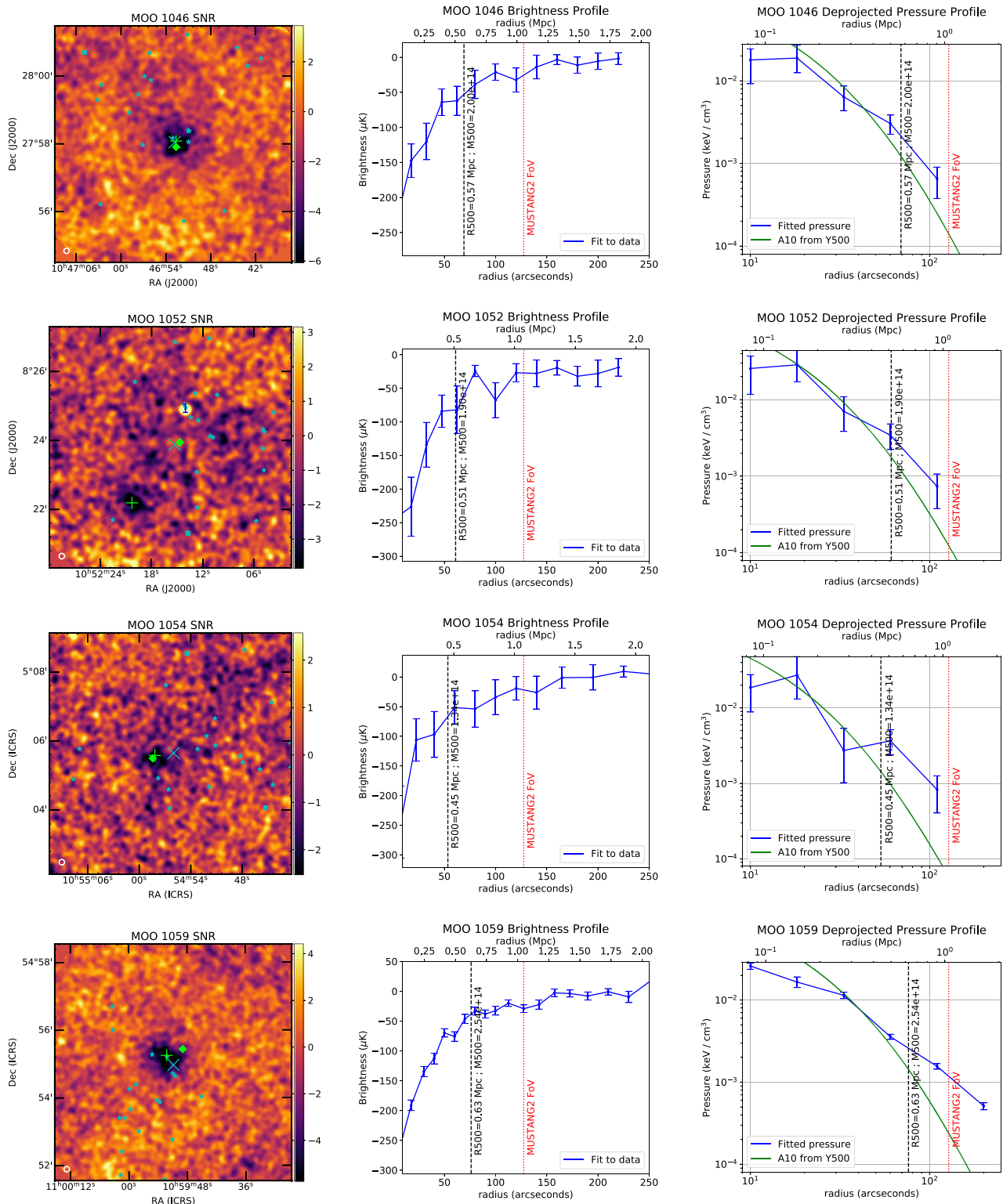


Figure 2. (Continued.)

masses ranging from $M_{500} = 10^{14}$ to $10^{15} M_{\odot}$ (corresponding to our expected mass range). Three different generalized Navarro–Frenk–White profiles were used as inputs. These were taken from Arnaud et al. (2010): an ensemble average “universal” profile, the average profile found to fit cool core

clusters, and the average profile found to fit disturbed clusters. Each profile was convolved with a $10''$ beam, then fake timestreams were generated by sampling these maps using the real observational scanning patterns used on the MaDCoWS clusters (Figure 1). Noise was added by taking MUSTANG2

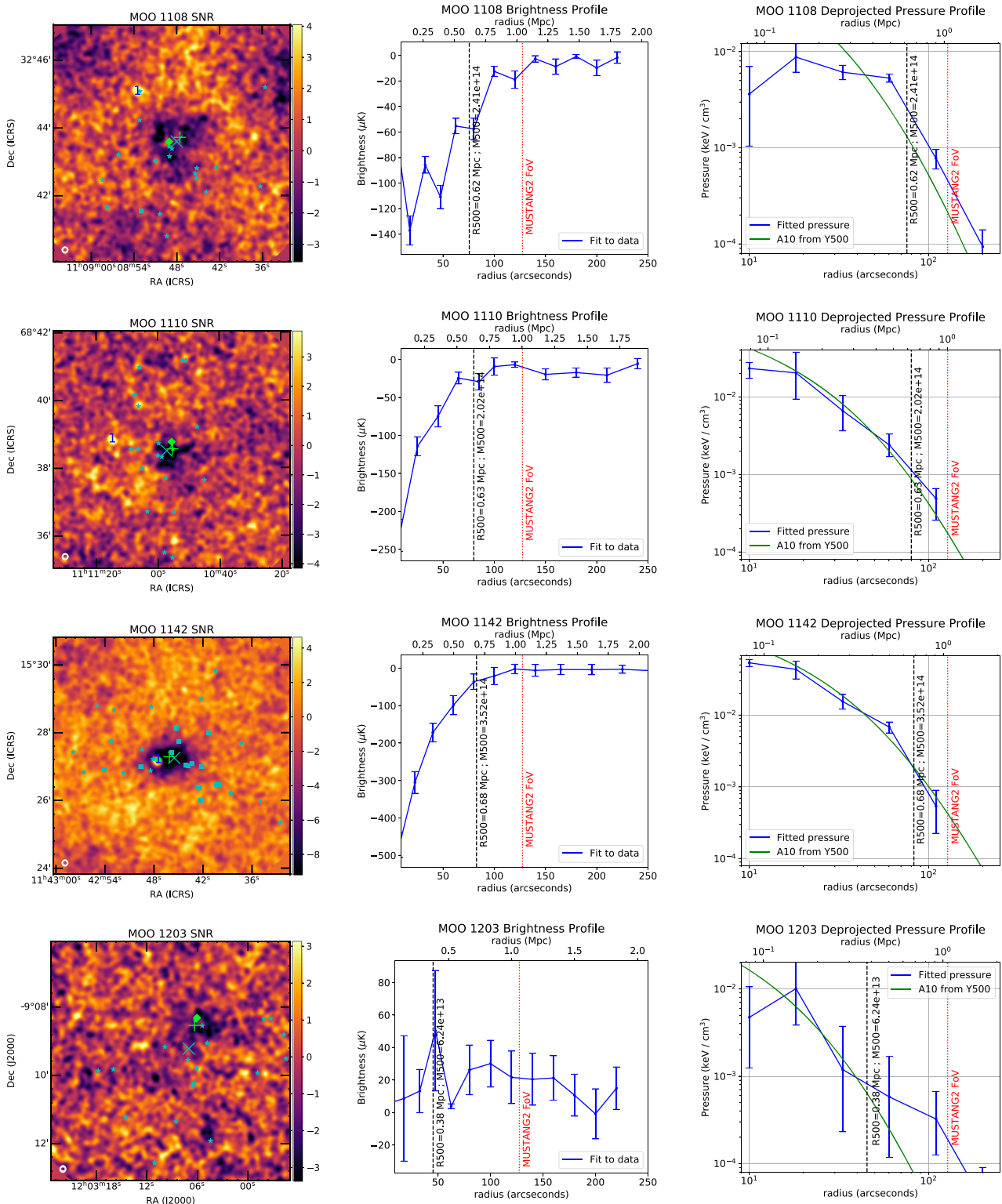


Figure 2. (Continued.)

timestreams from other RA projects that had observed blank fields and the data were analyzed using the same steps described in Section 3.

Initial simulations used the telescope pointings/scans for MOO 0105. These showed good recovery of the surface brightness profiles, the cluster pressure profile, and the cluster

mass for all redshifts, masses, and profiles chosen. However, when the same tests were carried out using the telescope pointings used for the blank fields the noise timestreams were taken from, less than half the original mass values were recovered and the surface brightness profiles showed significant errors of the order of $500 \mu\text{K}$. Further investigation

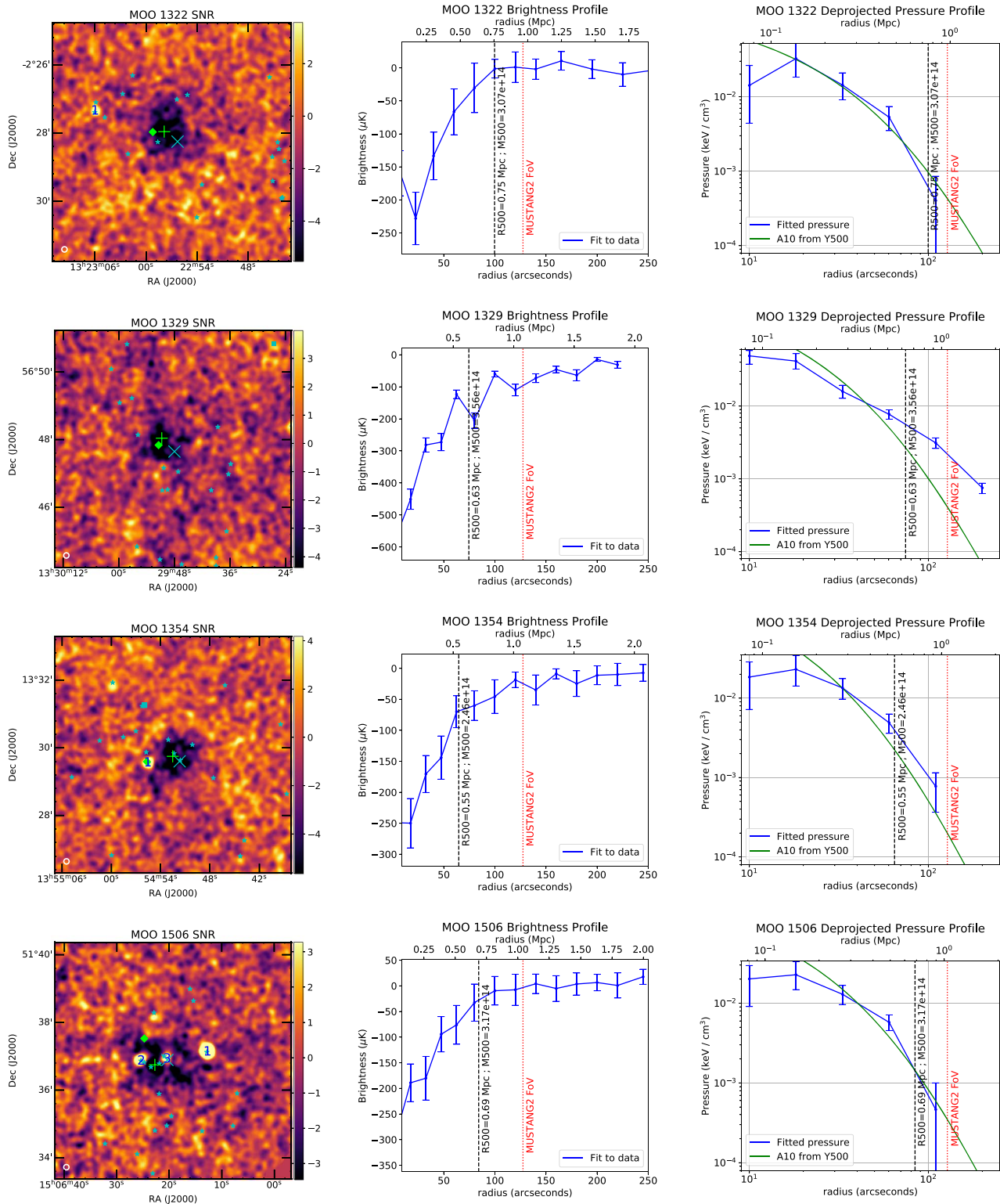


Figure 2. (Continued.)

showed that this was due to residual atmospheric gradients—when timestreams from one set of scans were used as noise in another, the phase of the atmospheric signal no longer matched that of the telescope scan pattern in elevation and was easily rejected as noise. When the same timestreams were used with the original telescope scan pattern and maps made in elevation/

cross-elevation then a residual atmospheric signal of the order of $100 \mu\text{K}$ remained in some maps. Due to sky rotation, maps made in R.A./decl. on a single pointing center sometimes produced circular features of the order $4'$ in diameter. To mitigate this, a second-order polynomial in the elevation direction around the scan center was fit for and subtracted from

Table 2
Fitted Point-source Locations and Amplitudes

Source ID	R.A.	Decl. (J2000)	Flux/mJy
MOO 0105:1	01:05:34.19	+13:23:06.7	0.493 ± 0.087
MOO 1031:1	10:32:04.10	+62:53:29.5	0.387 ± 0.038
MOO 1052:1	10:52:14.05	+08:24:54.2	0.511 ± 0.064
MOO 1054:1	10:54:59.33	+05:01:09.0	5.097 ± 0.277
MOO 1054:2	10:54:40.61	+05:07:36.3	0.679 ± 0.150
MOO 1108:1	11:08:53.50	+32:45:04.9	0.121 ± 0.026
MOO 1110:1	11:11:14.79	+68:38:51.9	0.173 ± 0.029
MOO 1142:1	11:42:47.48	+15:27:12.4	4.051 ± 0.035
MOO 1322:1	13:23:05.98	-02:27:21.2	0.353 ± 0.096
MOO 1354:1	13:54:55.57	+13:29:33.1	0.585 ± 0.068
MOO 1506:1	15:06:12.72	+51:37:07.7	3.489 ± 0.064
MOO 1506:2	15:06:25.34	+51:36:51.5	0.729 ± 0.052
MOO 1506:3	15:06:20.40	+51:36:55.1	0.553 ± 0.063
MOO 1506:4	15:05:55.55	+51:36:23.8	1.284 ± 0.149

Note. The number after each source ID refers to the source number designation in Figure 2. Source identifications are grouped by cluster field. A few sources are close to the edge of the maps and are not plotted in Figure 2.

each scan, after which our simulations showed accurate mass recovery for single pointing observations. These extra fit parameters (one set of second-order polynomial coefficients for each scan) were added to parameters in the Minkasi surface brightness fitting procedure described in Section 3.2 and used on all our real data. To make this more robust, in later observations, instead of a single pointing centered on the cluster four separate pointing centers around each cluster were used, each offset by $\pm 1'.5$ in R.A. or decl. Although this resulted in slightly less integration time on source, the improved ability to reject atmospheric noise more than made up for this.

As well as testing the recovery of cluster mass with different simulated cluster shapes, our sensitivity to errors in finding the cluster centers was tested. It was found that manually adding offsets of $30''$ to the centers of the clusters found by the first step of our pipeline had a negligible effect on the masses recovered. Also, changing the range of the fits between $180''$ and $240''$ changed the recovered masses by only a small fraction of the measurement error.

5. Results

Maps produced using the MIDAS pipeline are shown in Figure 2 along with pressure fits from Minkasi. Masses derived from these fits are shown in Table 3 along with derived values for Y_{500} and R_{500} . Out of our initial sample of 16 clusters, 14 show significant detections of the ICM. For the remaining two (MOO 1031 and MOO 1203), the noise in the maps is similar to that for the other clusters, allowing us to place strong upper limits on the masses ($\leq 1.3 \times 10^{14} M_{\odot}$ at 3σ) and there is a weaker (3.7σ) detection of the ICM.

Of the three clusters in this paper with both MUSTANG2 and CARMA mass measurements, two (MOO 0105 and MOO 1014) are in good agreement (see Figure 3). However, the MUSTANG2 mass for MOO 1142 is almost 40% below the CARMA value. Major differences between the CARMA and MUSTANG2 measurements are CARMA's $37''$ resolution and that the CARMA masses were obtained by directly fitting an A10 model to the interferometric observations, while in this paper the initial fit is nonparametric. Also Gonzalez et al.

(2015) found a $41''$ offset between their SZE center and the MaDCoWS center while with MUSTANG2 this offset was less than $10''$. One possible explanation for the difference in recovered masses is that MOO 1142 has two halos, and that MUSTANG2 has only fit for the largest, though no second halo is apparent in Figure 2 there are hints of a bimodal distribution of the WISE galaxy densities in (Figure 6 in Appendix B). Ruppin et al. (2020) recently published observations of this cluster using NIKA2 ($18''$ resolution at 150 GHz). Using X-ray data and the galaxy distribution they conclude that this cluster is an early stage merger (before first core passage). A similar combined analysis of the MUSTANG2 data will be investigated in future work.

The fitted SZE centers of the clusters are given in Table 4. Both the fitted SZE centers from this paper and the MaDCoWS centers from Gonzalez et al. (2019) have formal errors less than $21''$. For most of the clusters, the differences between these centers are less than $1'$ so they are consistent with each other. The exceptions are MOO 1031 (although this cluster has a low S/N) and MOO 1052. Subsequent reexamination of the WISE galaxy density for MOO 1052 shows a second peak in the galaxy density closer to the fitted SZE center (see Figure 6 in Appendix B). This could indicate an ongoing merger or it could be the result of contamination by foreground/background galaxies. Follow-up studies (e.g., X-ray or deeper SZE observations, or to obtain gravitational lensing and galaxy dynamics) would be of interest.

When compared to an A10 pressure profile, many of the clusters in Figure 2 show a shallower slope with the pressures being systematically higher above a radius of $100''$. At masses around $10^{14} M_{\odot}$ (where detections are marginal), the simulations typically recovered shallower profiles. However, at larger masses, the simulations showed that our pipeline recovered the correct profiles. Of our observed clusters with an S/N over 6σ , MOO 1046, MOO 1059, and MOO 1329 have a significantly shallower profile than A10, possibly indicating disturbance in the ICM or a possible merger.

Another feature in some of our recovered profiles is significantly lower pressure in the central $r \sim 25''$. MOO 0105, MOO 0135, MOO 1108, MOO 1354, and MOO 1506 are the five strongest examples. Again, this was not seen in recovered profiles from simulations and tests to see if using the incorrect beam size to recover the profiles could not reproduce this effect. The only way it was reproduced in simulations was by the introduction of large ($>30''$) errors in the fitted cluster centers. The maps in Figure 2 clearly show that the SZE centers match up to the decrements far better than this. However, looking at these maps, these clusters also show features at their centers. Active AGNs, low significance sources of any type, or a disturbed profile due to an ongoing merger could all cause such features. Comparison with other data sets will be explored in future papers.

6. The Mass-richness Relationship

Optical surveys for clusters of galaxies often employ some form of richness measure as a proxy for cluster mass (e.g., Abell 1958; Rykoff et al. 2012; Andreon 2015; Saro et al. 2015; Geach & Peacock 2017; Simet et al. 2017; Rettura et al. 2018; Chiu et al. 2020). For MaDCoWS, Gonzalez et al. (2019) defined the measure λ_{15} to be the excess number density of galaxies selected by Spitzer color cuts as possible cluster members with a brightness cutoff of $15 \mu\text{Jy}$. This flux cutoff

Table 3
Cluster Richness, Masses, and Size

Cluster ID	MaDCoWS ID	Richness ^a λ_{15}	M_{500c} (CARMA) ^a ($10^{14}M_{\odot}$)	M_{500c} (M2) ^b ($10^{14}M_{\odot}$)	Y_{500} (Mpc^2)	R_{500} (Mpc)	Notes
MOO 0105	MOO J0105+1323	87 ± 10	3.9 ± 0.5	$3.83^{+0.23,0.13,0.28}_{-0.24,0.12,0.26}$	2.77×10^{-5}	0.72	merger ^c
MOO 0135	MOO J0135+3207	39 ± 6	...	$1.82^{+0.31,0.07,0.13}_{-0.31,0.07,0.12}$	0.74×10^{-5}	0.50	
MOO 1014	MOO J1014+0038	44 ± 7	3.2 ± 0.35	$3.12^{+0.16,0.10,0.23}_{-0.15,0.10,0.24}$	1.93×10^{-5}	0.65	
MOO 1031	MOO J1031+6255	50 ± 7	...	$0.67^{+0.26,0.05,0.05}_{-0.26,0.05,0.05}$	0.13×10^{-5}	0.37	low S/N
MOO 1046	MOO J1046+2757	52 ± 7	...	$2.00^{+0.21,0.07,0.14}_{-0.23,0.07,0.14}$	0.87×10^{-5}	0.57	flat profile
MOO 1052	MOO J1052+0823	42 ± 6	...	$1.90^{+0.31,0.07,0.14}_{-0.35,0.07,0.13}$	0.80×10^{-5}	0.51	
MOO 1054	MOO J1054+0505	42 ± 6	...	$1.34^{+0.33,0.07,0.10}_{-0.34,0.06,0.09}$	0.43×10^{-5}	0.45	
MOO 1059	MOO J1059+5454	57 ± 7	...	$2.54^{+0.06,0.08,0.19}_{-0.06,0.08,0.17}$	1.34×10^{-5}	0.63	flat profile
MOO 1108	MOO J1108+3242	63 ± 8	...	$2.41^{+0.19,0.08,0.16}_{-0.20,0.08,0.16}$	1.22×10^{-5}	0.62	
MOO 1110	MOO J1110+6838	55 ± 7	...	$2.02^{+0.16,0.07,0.15}_{-0.16,0.07,0.14}$	0.89×10^{-5}	0.63	
MOO 1142	MOO J1142+1527	58 ± 8	5.7 ± 0.5	$3.52^{+0.19,0.11,0.26}_{-0.19,0.11,0.24}$	2.39×10^{-5}	0.68	merger
MOO 1203	MOO J1203-0909	56 ± 7	...	$0.64^{+0.26,0.05,0.05}_{-0.26,0.05,0.05}$	0.11×10^{-5}	0.37	low S/N
MOO 1322	MOO J1322-0228	83 ± 9	...	$3.07^{+0.41,0.10,0.22}_{-0.53,0.09,0.21}$	1.88×10^{-5}	0.75	
MOO 1329	MOO J1329+5647	42 ± 6	...	$3.56^{+0.20,0.12,0.26}_{-0.20,0.11,0.24}$	2.43×10^{-5}	0.63	flat profile
MOO 1354	MOO J1354+1329	44 ± 6	...	$2.46^{+0.25,0.08,0.18}_{-0.30,0.08,0.17}$	1.26×10^{-5}	0.55	
MOO 1506	MOO J1506+5136	74 ± 8	...	$3.17^{+0.29,0.10,0.22}_{-0.29,0.09,0.21}$	1.98×10^{-5}	0.69	merger ^c

Notes.

^a Richness and mass values from Gonzalez et al. (2019). More information on MOO 1506 can be found in Moravec et al. (2020).

^b The errors on the MUSTANG2 masses are, from left to right, the statistical errors, errors due to the Y–M relationship, and errors due to the absolute calibration of MUSTANG2 data.

^c Merger status of MOO 0105 and MOO 1506 are based on X-ray morphologies in Chandra imaging, (Gonzalez et al. 2019) and MOO 1142 is claimed to be a merger in Ruppin et al. (2020).

corresponds to a stellar mass of $\sim 5 \times 10^{10} M_{\odot}$. An aperture of 1 Mpc in radius was used for the calculation. To calibrate the $M_{500} - \lambda_{15}$ scaling relation, masses determined using 14 SZE observations from CARMA were used. The CARMA sample included MOO 0105 and MOO 1142, which are also present in the sample studied here using MUSTANG2. A fit for the relationship between λ_{15} and M_{500} with the assumed form:

$$\log_{10} \frac{M_{500}}{10^{14}M_{\odot}} = \alpha \log_{10} \lambda_{15} + \beta + \eta$$

was made where α and β are the slope and intercept of the relation, respectively. The term η takes into account any scatter inherent to the data points with respect to the reconstructed linear relation (i.e., intrinsic scatter), and is assumed to be a Gaussian random variable with variance $\sigma_{\log M|\lambda}^2$ and a null expectation value. Clusters with twice as many galaxies can be expected to be approximately twice as massive so values of α close to unity are expected (e.g., Andreon & Hum 2010; Chiu et al. 2020). The Bayesian linear regression algorithm `linmix` (Kelly 2007) was used for the fit in Gonzalez et al. (2019). Although `linmix` does not fully account for scatter in the x parameter (and so can produce biased results), for consistency, we use the same method but include the MUSTANG2 SZE-inferred masses presented in this paper and those inferred from ACA observations (Di Mascolo et al. 2020).

A plot of the mass-richness data can be seen in Figure 3 and plots of some of the fits can be seen in Figure 4. More plots of fits along with a table of parameters can be found in Appendix B. Gonzalez et al. (2019) excluded known mergers from their fits and found best-fit values of $\alpha = 1.65^{+1.45}_{-0.96}$ and $\beta = -2.16^{+1.57}_{-2.38}$ with a large scatter of $\sigma_{\log M|\lambda} = 0.12$. Adding

in data from the ACA lowers the slope only slightly (to $\alpha = 1.41^{+2.42}_{-1.70}$) but the change in the offset is larger (to $\beta = -1.88^{+2.81}_{-4.01}$) and as noted in Di Mascolo et al. (2020), the scatter increases. This is consistent with the fact that ACA clusters that are not known mergers or upper limits are spread over a relatively narrow range of richness ($40 < \lambda_{15} < 55$) so they cannot constrain the slope well. They also lie below the CARMA data (Figure 3).

A fit to the MUSTANG2 clusters (excluding known mergers MOO 0105, MOO 1142, and MOO 1506 and low S/N clusters MOO 1031 and MOO 1203) has a significantly shallower slope ($\alpha = 0.30^{+0.76}_{-0.68}$), a higher intercept ($\beta = -0.13^{+1.16}_{-1.30}$), but comparable scatter to the CARMA/ACA fits. The inclusion of low S/N clusters has only a small effect on the fitted slopes with the main effect to be an increase in the scatter. Although including upper limits in the fits increases the scatter, it is important to do so if one wants to avoid biasing results—for example, if a significant number of high richness clusters had far lower SZE masses than expected and were not detected then only fitting the detections would bias the slope high. Information on nondetections in the CARMA observations is not given in Gonzalez et al. (2019) and the authors caution that a more complete analysis of the CARMA fits to include the nondetections is needed. If some of these nondetections were high richness clusters with a much lower than expected flux, the exclusion of these data points would bias a fit to the CARMA data to a steeper slope.

Figure 3 shows hints that the population of galaxy clusters could exhibit a break or bimodality, with nonmergers following the steeper CARMA fit, and mergers falling significantly below that relation and closer to the flatter MUSTANG2 fit. To first order, the number of galaxies above a given flux would be

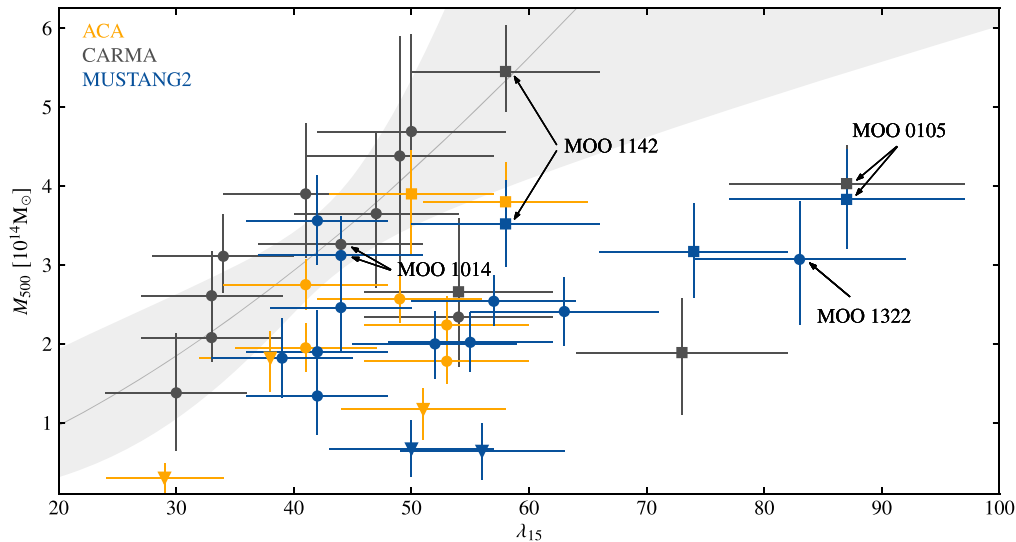


Figure 3. SZE-inferred masses from three instruments/observatories that have targeted samples of 10 or more MaDCoWS clusters plotted against their richness reported in Gonzalez et al. (2019). The black, orange, and blue points are from CARMA, the ACA, and MUSTANG2 (this paper) respectively. The mass-richness relation (with errors) that was fitted to the CARMA data in Gonzalez et al. (2019) is shown as the gray line and shaded region. Low significant points are indicated by triangles, and the known mergers (from Gonzalez et al. 2019; Ruppin et al. 2020) are depicted as squares. The circles represent all other clusters. All errors are 1σ .

Table 4
Fitted SZE Centers

Cluster ID	R.A. (J2000)	Decl. (J2000)	SZE Offset ($''$)
MOO 0105	01:05:31.30	+13:24:00.1	(12.8, -1.8)
MOO 0135	01:35:02.44	+32:07:41.4	(-28.0, 14.2)
MOO 1014	10:14:07.18	+00:38:18.2	(-4.7, -12.0)
MOO 1031	10:32:01.56	+62:54:53.9	(200.0, -36.6)
MOO 1046	10:46:52.63	+27:58:05.0	(-2.8, 2.1)
MOO 1052	10:52:20.31	+08:22:11.4	(75.1, -101.6)
MOO 1054	10:54:58.18	+05:05:34.8	(32.6, -4.2)
MOO 1059	10:59:52.21	+54:55:15.2	(20.7, 16.8)
MOO 1108	11:08:47.56	+32:43:43.3	(-6.6, 7.5)
MOO 1110	11:10:55.29	+68:38:33.9	(-27.9, 3.2)
MOO 1142	11:42:46.12	+15:27:17.4	(9.1, 2.0)
MOO 1203	12:03:06.33	-09:08:32.2	(-10.0, 40.8)
MOO 1322	13:22:57.87	-02:27:57.4	(23.5, 17.6)
MOO 1329	13:29:50.73	+56:48:02.6	(41.0, 23.6)
MOO 1354	13:54:52.54	+13:29:44.9	(12.6, 8.9)
MOO 1506	15:06:22.74	+51:36:44.9	(35.8, -8.7)

Note. Offsets are given separately in R.A. and decl. from the MaDCoWS galaxy overdensity center.

unchanged during a merger so as soon as the two merging clusters are within the line-of-sight radius in which richness is being measured then the richness value should increase to close to the value for the new combined cluster. Richness, including λ_{15} used in this paper, should be relatively unaffected by the dynamical state of a post-merger cluster. The intrinsic scatter in mass-richness relations is less certain with values between 15% and 50% being quoted depending on the exact definition of richness (for examples, see Andreon & Hum 2010; Andreon 2015). The intrinsic scatter in the Y–M relation for the SZE is known to be lower at around 10%. However, during a merger individual clusters can vary by more than this. Simulations show a brief enhancement in the SZE signal during the first core passage and then less SZE signal by up to 40% until the gas in the ICM has virialized or thermalized in the merged gravitational potential (Wik et al. 2008; Marrone et al. 2012). Empirical studies have generally confirmed this (e.g.,

Bocquet et al. 2015; Hilton et al. 2018). Consequently one would expect that including merging clusters when using the SZE to calibrate a mass-richness scaling relation would result in a more shallow slope (see in addition the discussion of mergers in Moravec et al. 2020).

To test if undetected mergers are driving the differences between the MUSTANG2 and CARMA slopes, the data were refit to include known mergers. The result is that the slope of all data sets became similar (0.5–0.9) but still slightly steeper than the slope from MUSTANG2 excluding mergers (0.30). We also note that known mergers dominate the high richness end of Figure 3, with the exception of MOO 1322, which has a median mass $M_{500} \approx 3.1 \times 10^{14} M_{\odot}$ and MaDCoWS richness $\lambda_{15} = 83$. Data points in this region of the plot are driving the fits toward flatter slopes. From the MUSTANG2 data alone (Figure 2), there is no conclusive evidence that MOO 1322 is a merger. However, in Figure 6 in Appendix A, we provide Spitzer/IRAC color-selected galaxy density maps with the MUSTANG2 SZE decrement contours overplotted. Although MOO 1322 has the second highest richness in our sample, it appears not to have a strong galaxy concentration when applying this color cut. This may be due to the galaxy members being bluer than expected for a virialized system, which would be consistent with the low SZE signal and likely imply this is an unvirialized, line-of-sight merger. We tested the effect of excluding MOO 1322 along with the known mergers from the scaling relation fits. Due to the narrow range of richness of the remaining data, this results in much poorer constraints on the slope of the fit to the MUSTANG2 data alone (Figure 4). Follow-up observations such as optical spectroscopy to verify if this cluster is a merger would be of interest and planned observations of more MaDCoWS clusters using MUSTANG2 over a wider range of richnesses (to fill in this region) will better constrain the scaling relation with or without this cluster. Given how much the MUSTANG2 fit is affected by this one cluster then until such observations are obtained the scaling relationship derived from MUSTANG2 data should be considered preliminary.

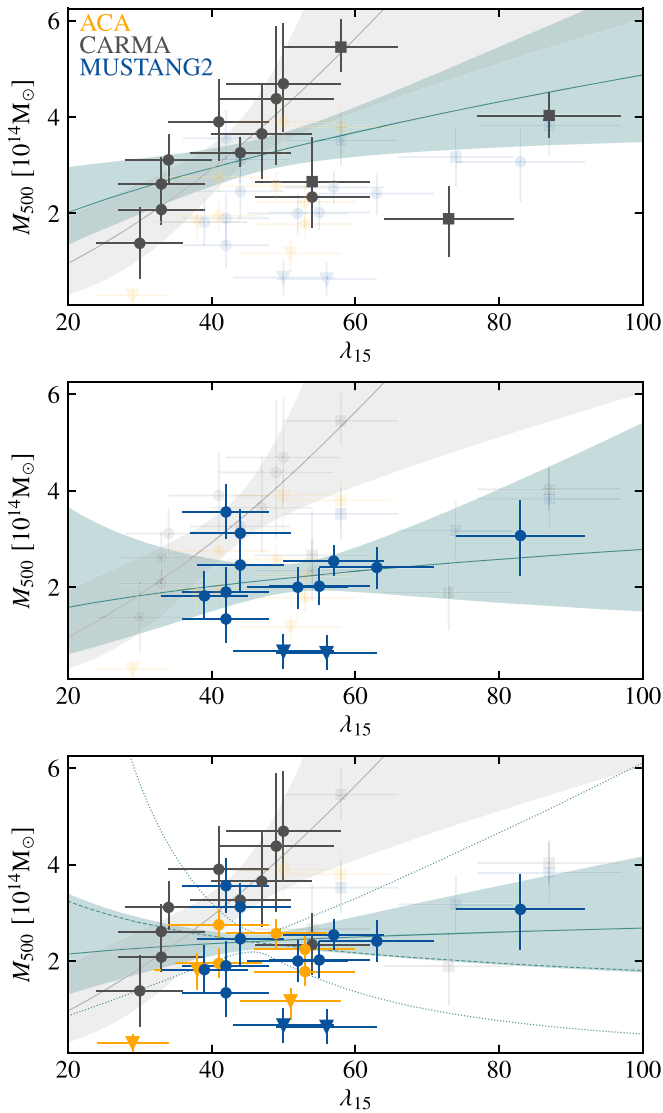


Figure 4. Mass-richness scaling relations obtained from different data sets. The data included/excluded from each of the fits are denoted with bold/faint markers (we refer to Figure 3 for more details about the notation). The best-fit relations are shown as green solid lines and the shaded areas represent the errors in the fits. As in Figure 3, the gray line and shaded region refer to the mass-richness relation reported in Gonzalez et al. (2019). Top: the effects of including known mergers in the CARMA fit. Middle: a fit to the MUSTANG2 data excluding known mergers. The dashed and dotted lines denote the best-fit relation and corresponding credibility interval obtained when excluding MOO 1322 (the richest nonmerging cluster in the MUSTANG2 MaDCoWS pilot sample). Bottom: a fit to all the data excluding known mergers.

Mergers per unit time are expected to be more common at high redshift (Fakhouri et al. 2010) so it is possible that several of the systems in this sample not currently thought to be mergers are in fact mergers. Ongoing mergers could explain why MOO 1031 and MOO 1203 have similar richnesses to many robustly detected clusters in the sample but are relatively weakly detected by MUSTANG2. The correct identification of which clusters are merging could become the limiting factor when finding an accurate mass-richness scaling relation using SZE observations. MUSTANG2’s ability to resolve structure within clusters could be of some use here—with the planned larger sample it will be possible to group clusters by their profile shapes and carry out searches for signs of shocks in the ICM. Other signs of mergers include double peaks in galaxy

distributions (either spatially for mergers in the plane of the sky or spectroscopically for mergers along the line of sight) and offsets between the SZE center and the center of the galaxies (for example, MOO 1052). When available, comparison with deep X-ray data could be used in a joint analysis (to obtain better temperature constraints than either data set alone) and X-ray masses compared to SZE masses.

7. Segmented Fits

The cluster profiles presented in Section 5 assume symmetry. However, through examination of the maps, we see some evidence that the cluster morphology is asymmetric (e.g., the center of MOO 1142), and at least three of the clusters are known mergers (where one might expect an asymmetric profile). The analysis in Section 3.2 was repeated but with the rings broken into four segments of 90° . An asymmetrical cluster with one axis aligned within the segments chosen (in the first round of analyses 0° , 90° , 180° , and 270° east of north) would show up as different profiles in some segments. To fully test for asymmetry this process was repeated for angles of 45° , 135° , 225° , and 315° . Examples of some of the fits are shown in Figure 5—within the errors no significant derivations from spherical symmetry could be detected in the brightness profiles and the masses recovered from each segment were the same to within the statistical error.

As a further check, the symmetrical profiles from Section 3.2 were subtracted from the maps (along with any point sources). In all cases the residual signal was consistent with zero. While this does not mean there is no asymmetry in the clusters, deeper maps would be needed to detect it. Asymmetry is a sign of possible mergers and mergers could have a dramatic effect on the mass-richness scaling relation (Section 6) so joint analysis using other data sets on the complete MUSTANG2 sample is planned. Other possible future avenues include using matched filters to search for small-scale features, such as shock fronts in the MUSTANG2 maps.

8. Conclusions

In this paper we have presented initial results of using MUSTANG2 to follow-up a pilot sample of clusters detected by the MaDCoWS project (for the full catalog, see Gonzalez et al. 2019). With integration times between two and seven hours on 16 clusters, we were able to detect, through the SZE effect, 14 of our targets and obtain robust estimates of their masses as well as measurements of their SZE brightness and pressure profiles. Strong upper limits on the masses of the other two were obtained. MUSTANG2’s $9''$ resolution ($10''$ after smoothing) makes the identification and removal of point sources from the observations relatively straightforward compared to smaller single dish and survey instruments. The cluster profiles and the offsets between the best-fit centers for the SZE compared with the MaDCoWS centers give indications of the dynamical states of our 14 detections. In general the fitted SZE centers agreed well with those identified in Gonzalez et al. (2019), and no strong evidence could be found for asymmetry in any of the clusters. However, in the case of MOO 1052 there is a significant ($>2'$) offset between the SZE and MaDCoWS centers, making this a good target for follow-up work to investigate whether it is undergoing a merger.

The mass-richness relationship derived using the MUSTANG2 MaDCoWS pilot sample alone, excluding known

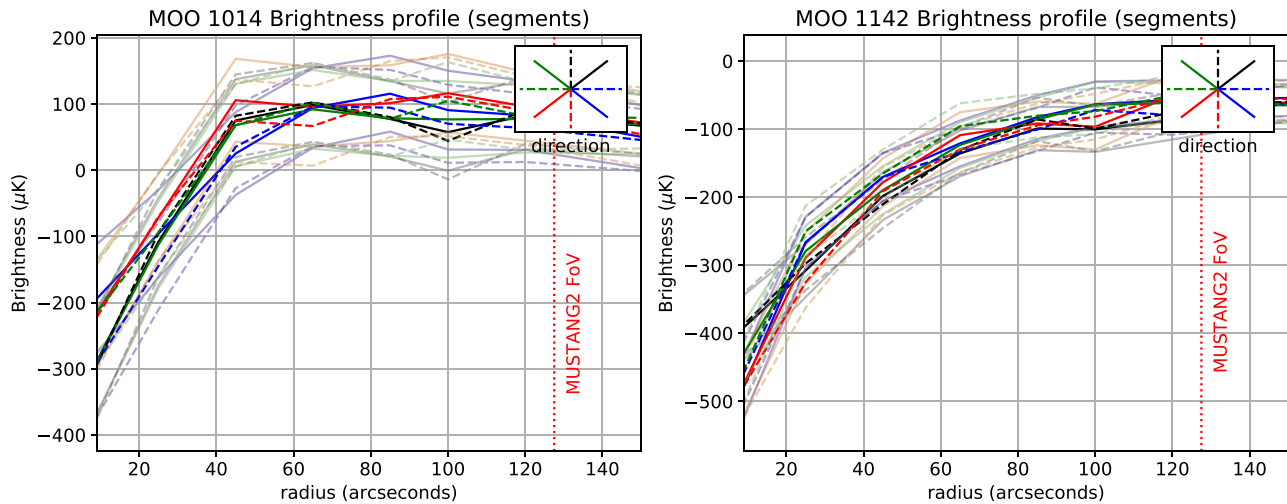


Figure 5. Cluster profiles fit over 90° slices. The solid and dashed lines represent the 90° slice directions shown in the top right of each plot while the fainter lines on either side show the 3σ error bars corresponding to that color and line style.

mergers but including upper limits, exhibits similar high scatter as those from CARMA and ACA data. However, the best-fit scaling relations to any data sets that include MUSTANG2 data are all significantly flatter than those derived for CARMA or CARMA+ACA, but still consistent with $\alpha = 1$. We note that the SZE observations with MUSTANG2 and ACA are in general deeper and higher resolution than those performed with CARMA, and posit that we may be probing previously unexplored parts of the MaDCoWS cluster population. We also note that the CARMA data excluded a number of weak and nondetections lying below their sensitivity limit, which could bias the inferred scaling relation in Gonzalez et al. (2019) to a steeper slope. Conversely the slope of the fit to the MUSTANG2 data is strongly leveraged by the inclusion of a single cluster, MOO 1322. The dynamical state of this cluster is uncertain and it could be biasing the inferred scaling relation from MUSTANG2 data to a flatter value—including mergers in the fits to ACA and CARMA data dramatically flattens these slopes as well. Further studies, such as the already-approved, upcoming MUSTANG2 observations, will be necessary to resolve the discrepancies in mass-richness relationships. In particular it will be important to include a greater number of MaDCoWS clusters spanning a wider range of richnesses and to ensure only those clusters known to be relaxed are used in the fit.

MUSTANG2 is supported by the NSF award number 1615604 and by the Mt. Cuba Astronomical Foundation. The National Radio Astronomy Observatory is a facility of the National Science Foundation operated under cooperative agreement by Associated Universities, Inc. GBT data was taken under

the project IDs AGBT18B_215 and AGBT19B_200. E.M. acknowledges the support of the EU-ARC.CZ Large Research Infrastructure grant project LM2018106 of the Ministry of Education, Youth and Sports of the Czech Republic. The work of T.C. and D.S. was carried out at the Jet Propulsion Laboratory, California Institute of Technology, under a contract with NASA. This paper made use of APLpy 2.0., an open-source plotting package for Python (Robitaille & Bressert 2012).

Facility: GBT (MUSTANG2).

Software: astropy (<https://www.astropy.org/>), APLpy (<https://aplpy.github.io/>).

Appendix A Galaxy Number Densities Inferred from Spitzer/ IRAC Data

In Figure 6, we present overlays of the SZE decrements on galaxy density maps inferred from Spitzer/IRAC observations. The galaxies are selected to be preferentially at the MaDCoWS redshifts using the same color cuts described in Gonzalez et al. (2019) and to be brighter than 15 mJy at a wavelength of $4.5 \mu\text{m}$. Overall there is good agreement between the optical and SZE images. Exceptions include our low S/N clusters, MOO 1031 (where there is very little sign of any SZE signal where the galaxy density is) and MOO 1203 (where the SZE signal is only detected on an off-centered peak in the bulk Spitzer galaxy overdensity). The SZE signal for MOO 1052 is centered on a second peak in the galaxy distribution, away from the MaDCoWS-identified center, indicating a possible merger or potential contamination from foreground/background galaxies.

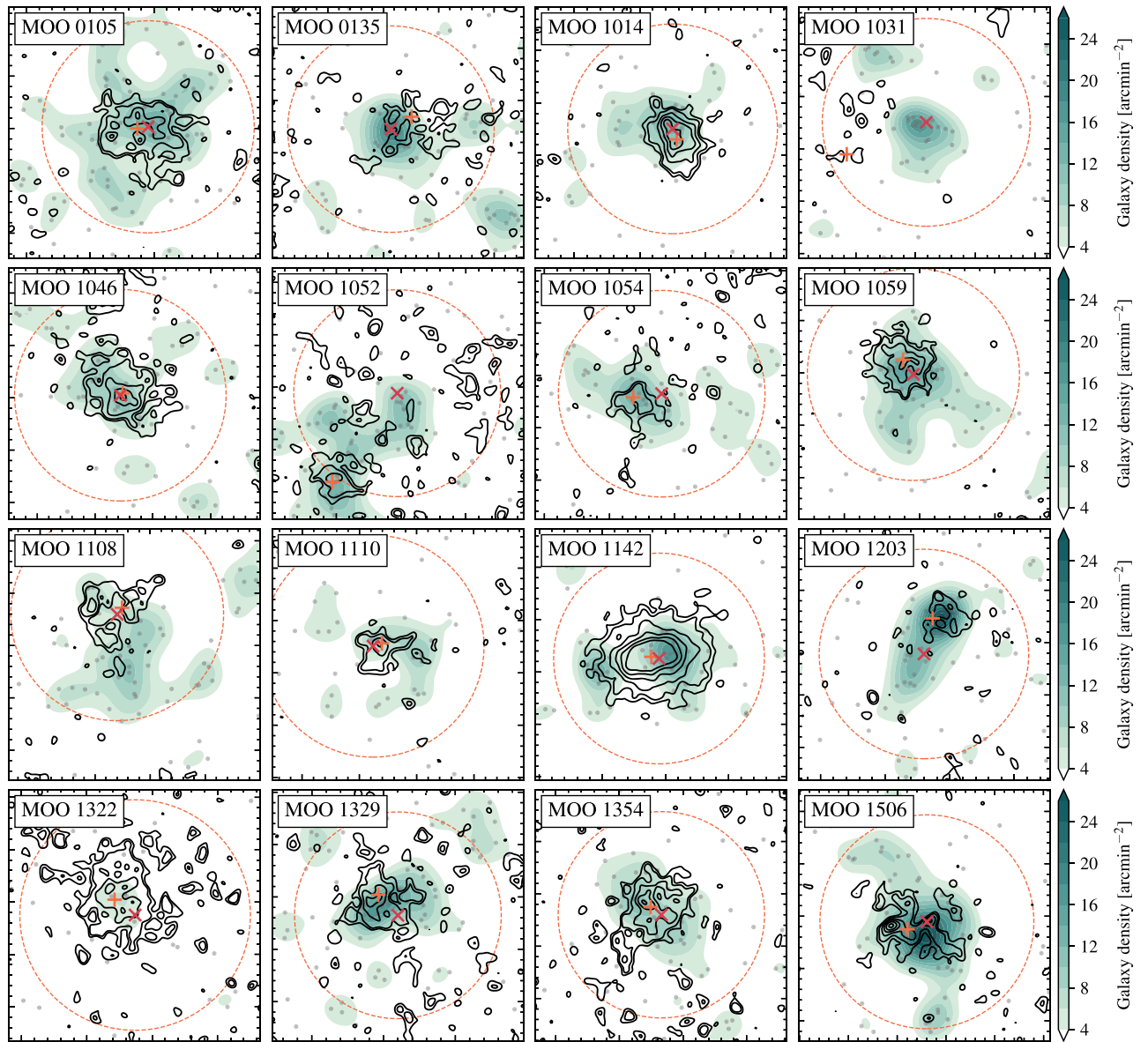


Figure 6. Spitzer/IRAC galaxy density maps. Galaxies are selected by color cuts to be preferentially in the redshift range 0.0–1.4 (see Wylezalek et al. 2014; Gonzalez et al. 2019, for details). The galaxy number densities are smoothed with a $40''$ FWHM Gaussian kernel. Each plot is $4'.8 \times 4'.8$. The MaDCoWS position (Table 1) is shown as a red X and the dashed red lines represent the 1 Mpc radius circle used to calculate λ_{15} . Point-source-subtracted contours from the MUSTANG2 S/N maps are overlaid in black, with contour levels of $-2, -3, -5, -7, -9,$ and -11σ . The fitted SZE centers are marked with an orange +.

Appendix B

Further Considerations for the SZE Mass versus Richness Scaling Relations

In Figure 7 and Table 5, we present results for the mass-richness ($M_{500} - \lambda_{15}$) scaling relations that we infer when

including or excluding various SZE observational data sets, known mergers, and weak or nondetections (i.e., upper limits).

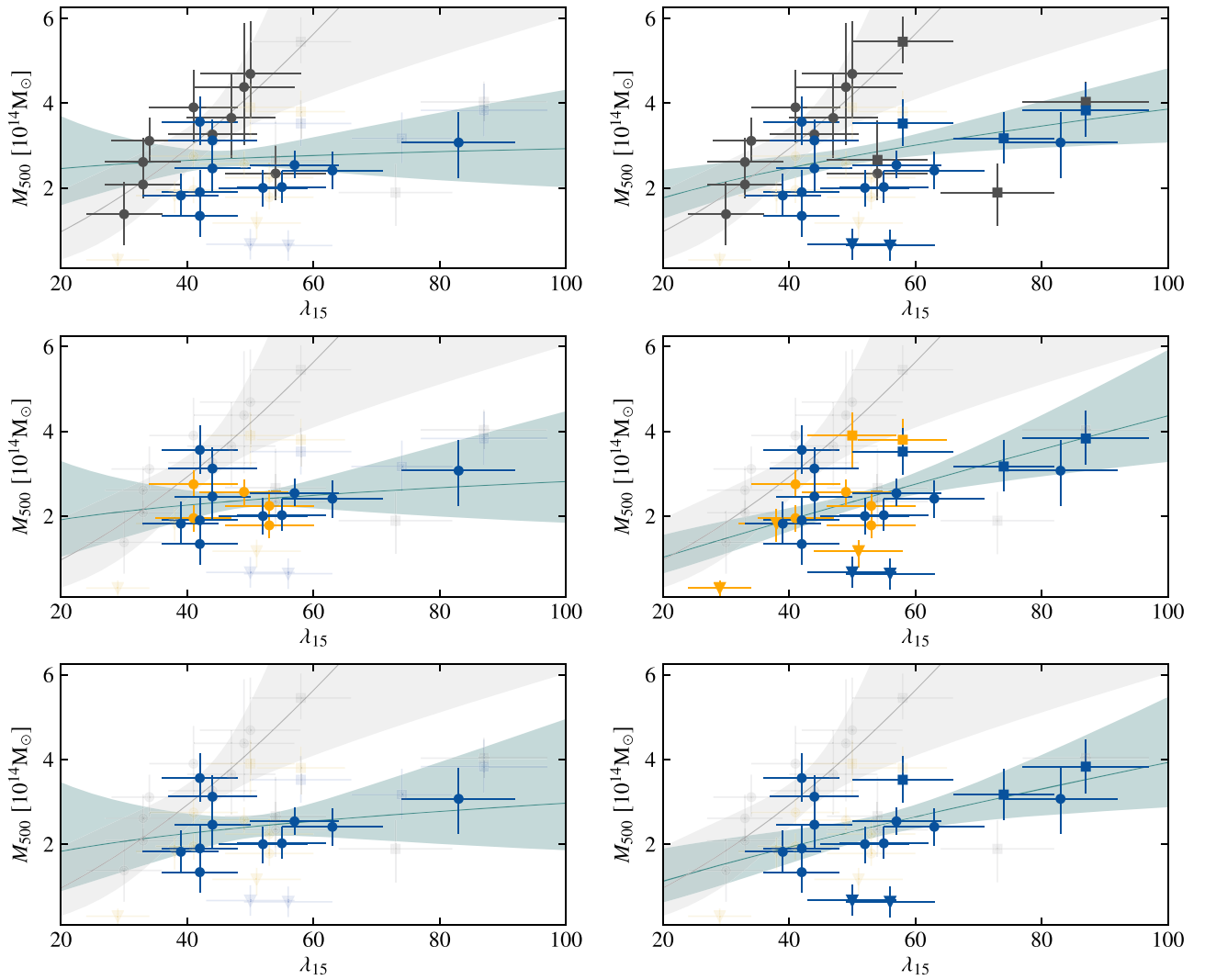










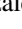




Figure 7. Plots of selected scaling relations reported in Table 5, including or excluding known mergers, weak or nondetections, and including or excluding the CARMA and ACA data (from Gonzalez et al. 2019 and Di Mascolo et al. 2020 respectively). The shaded gray region in each plot is the fit to the CARMA points only (including 1σ error bars), while each color region shows the mass-richness scaling relation appropriate for the data points in bold, which are (upper left) fit to MUSTANG2+CARMA data, excluding known mergers and weak/nondetections; (upper right) fit to MUSTANG2+CARMA data, including known mergers and weak/nondetections; (middle left) fit to MUSTANG2+ACA data, excluding known mergers and weak/nondetections; (middle right) fit to MUSTANG2+ACA data, including known mergers and weak/nondetections; (lower left) fit to MUSTANG2 data alone, excluding known mergers and weak/nondetections; and (lower right) fit to MUSTANG2 data alone, including known mergers and weak/nondetections. The exclusion of known mergers and low significance detection and nondetections does not reconcile the scaling relations when including MUSTANG2 data with those found fitting the CARMA detections alone.

Table 5
Fits for Mass-richness Scaling Relations

SZE Data Used	α	β	$\sigma_{\log M \lambda}$
Excluding known mergers and nondetections			
CARMA	$1.65^{+1.45}_{-0.96}$	$-2.16^{+1.57}_{-2.38}$	0.12
CARMA+ACA	$0.07^{+0.51}_{-0.50}$	$0.29^{+0.83}_{-0.86}$	$0.15^{+0.01}_{-0.00}$
MUSTANG2 (M2)	$0.30^{+0.76}_{-0.68}$	$-0.13^{+1.16}_{-1.30}$	$0.14^{+0.03}_{-0.01}$
M2+CARMA	$0.11^{+0.51}_{-0.48}$	$0.26^{+0.79}_{-0.86}$	$0.16^{+0.02}_{-0.00}$
M2+ACA	$0.24^{+0.67}_{-0.59}$	$-0.02^{+1.01}_{-1.13}$	$0.12^{+0.02}_{-0.01}$
M2+CARMA+ACA	$0.06^{+0.52}_{-0.50}$	$0.30^{+0.83}_{-0.88}$	$0.15^{+0.02}_{-0.00}$
Excluding known mergers including nondetections			
CARMA
CARMA+ACA	$0.13^{+0.58}_{-0.56}$	$0.16^{+0.94}_{-0.97}$	$0.27^{+0.01}_{-0.01}$
MUSTANG2 (M2)	$0.35^{+0.99}_{-0.89}$	$-0.26^{+1.52}_{-1.69}$	$0.27^{+0.02}_{-0.00}$
M2+CARMA	$0.01^{+0.58}_{-0.56}$	$0.40^{+0.94}_{-0.96}$	$0.24^{+0.01}_{-0.00}$
M2+ACA	$0.51^{+0.76}_{-0.67}$	$-0.53^{+1.13}_{-1.29}$	$0.28^{+0.02}_{-0.01}$
M2+CARMA+ACA	$0.15^{+0.57}_{-0.55}$	$0.14^{+0.91}_{-0.95}$	$0.27^{+0.01}_{-0.01}$
Including known mergers excluding nondetections			
CARMA	$0.54^{+0.44}_{-0.42}$	$-0.40^{+0.71}_{-0.73}$	$0.17^{+0.02}_{-0.00}$
CARMA+ACA	$0.55^{+0.30}_{-0.28}$	$-0.49^{+0.49}_{-0.52}$	$0.15^{+0.01}_{-0.00}$
MUSTANG2 (M2)	$0.63^{+0.45}_{-0.41}$	$-0.68^{+0.72}_{-0.78}$	$0.12^{+0.02}_{-0.00}$
M2+CARMA	$0.47^{+0.29}_{-0.29}$	$-0.34^{+0.50}_{-0.51}$	$0.16^{+0.01}_{-0.00}$
M2+ACA	$0.69^{+0.42}_{-0.38}$	$-0.78^{+0.66}_{-0.73}$	$0.12^{+0.01}_{-0.00}$
M2+CARMA+ACA	$0.56^{+0.30}_{-0.30}$	$-0.50^{+0.52}_{-0.51}$	$0.15^{+0.01}_{-0.00}$
Including known mergers including nondetections			
CARMA
CARMA+ACA	$0.65^{+0.33}_{-0.32}$	$-0.68^{+0.54}_{-0.56}$	$0.25^{+0.01}_{-0.00}$
MUSTANG2 (M2)	$0.77^{+0.56}_{-0.50}$	$-0.95^{+0.88}_{-0.98}$	$0.25^{+0.01}_{-0.00}$
M2+CARMA	$0.49^{+0.33}_{-0.32}$	$-0.39^{+0.56}_{-0.56}$	$0.23^{+0.01}_{-0.00}$
M2+ACA	$0.90^{+0.46}_{-0.42}$	$-1.16^{+0.72}_{-0.79}$	$0.26^{+0.01}_{-0.01}$
M2+CARMA+ACA	$0.65^{+0.33}_{-0.32}$	$-0.69^{+0.56}_{-0.56}$	$0.25^{+0.01}_{-0.00}$

ORCID iDs

Simon R. Dicker  <https://orcid.org/0000-0002-1940-4289>
 Charles E. Romero  <https://orcid.org/0000-0001-5725-0359>
 Luca Di Mascolo  <https://orcid.org/0000-0003-3586-4485>
 Tony Mroczkowski  <https://orcid.org/0000-0003-3816-5372>
 Jonathan Sievers  <https://orcid.org/0000-0001-6903-5074>
 Emily Moravec  <https://orcid.org/0000-0001-9793-5416>
 Mark Brodwin  <https://orcid.org/0000-0002-4208-798X>
 Thomas Connor  <https://orcid.org/0000-0002-7898-7664>
 Mark Devlin  <https://orcid.org/0000-0002-3169-9761>
 Anthony H. Gonzalez  <https://orcid.org/0000-0002-0933-8601>
 Brian S. Mason  <https://orcid.org/0000-0002-8472-836X>
 Craig Sarazin  <https://orcid.org/0000-0003-0167-0981>
 Daniel Stern  <https://orcid.org/0000-0003-2686-9241>

Dominika Wylezalek  <https://orcid.org/0000-0003-2212-6045>

References

- Abell, G. O. 1958, *ApJS*, 3, 211
 Allen, S. W., Evrard, A. E., & Mantz, A. B. 2011, *ARA&A*, 49, 409
 Andreon, S. 2015, *A&A*, 582, A100
 Andreon, S., & Hurn, M. A. 2010, *MNRAS*, 404, 1922
 Arnaud, M., Pratt, G. W., Piffaretti, R., et al. 2010, *A&A*, 517, A92
 Bleem, L. E., Bocquet, S., Stalder, B., et al. 2020, *ApJS*, 247, 25
 Bleem, L. E., Stalder, B., de Haan, T., et al. 2015, *ApJS*, 216, 27
 Bocquet, S., Saro, A., Mohr, J. J., et al. 2015, *ApJ*, 799, 214
 Brodwin, M., Greer, C. H., Leitch, E. M., et al. 2015, *ApJ*, 806, 26
 Bulbul, E., Chiu, I. N., Mohr, J. J., et al. 2019, *ApJ*, 871, 50
 Carlstrom, J. E., Holder, G. P., & Reese, E. D. 2002, *ARA&A*, 40, 643
 Castagna, F., & Andreon, S. 2020, *A&A*, 639, A73
 Chiu, I.-N., Okumura, T., Oguri, M., et al. 2020, *MNRAS*, 498, 2030
 Churazov, E., Vikhlinin, A., & Sunyaev, R. 2015, *MNRAS*, 450, 1984
 Cruddace, R., Voges, W., Böhringer, H., et al. 2002, *ApJS*, 140, 239
 Di Mascolo, L., Mroczkowski, T., Churazov, E., et al. 2020, *A&A*, 638, A70
 Dicker, S. R., Ade, P. A. R., Aguirre, J., et al. 2014, *JLTP*, 176, 808
 Dünner, R., Hasselfield, M., Marriage, T. A., et al. 2013, *ApJ*, 762, 10
 Fakhouri, O., Ma, C.-P., & Boylan-Kolchin, M. 2010, *MNRAS*, 406, 2267
 Fassbender, R., Böhringer, H., Nastasi, A., et al. 2011, *NJPh*, 13, 125014
 Foreman-Mackey, D., Hogg, D. W., Lang, D., & Goodman, J. 2013, *PASP*, 125, 306
 Ge, C., Sun, M., Rozo, E., et al. 2019, *MNRAS*, 484, 1946
 Geach, J. E., & Peacock, J. A. 2017, *NatAs*, 1, 795
 Gonzalez, A. H., Decker, B., Brodwin, M., et al. 2015, *ApJL*, 812, L40
 Gonzalez, A. H., Gettings, D. P., Brodwin, M., et al. 2019, *ApJS*, 240, 33
 Hasselfield, M., Hilton, M., Marriage, T. A., et al. 2013, *JCAP*, 2013, 008
 Hilton, M., Hasselfield, M., Sifón, C., et al. 2018, *ApJS*, 235, 20
 Holz, D. E., & Perlmuter, S. 2012, *ApJL*, 755, L36
 Huang, N., Bleem, L. E., Stalder, B., et al. 2020, *AJ*, 159, 110
 Itoh, N., Kohyama, Y., & Nozawa, S. 1998, *ApJ*, 502, 7
 Kelly, B. C. 2007, *ApJ*, 665, 1489
 Korngut, P. M., Dicker, S. R., Reese, E. D., et al. 2011, *ApJ*, 734, 10
 Marriage, T. A., Acquaviva, V., Ade, P. A. R., et al. 2011, *ApJ*, 737, 61
 Marrone, D. P., Smith, G. P., Okabe, N., et al. 2012, *ApJ*, 754, 119
 Mason, B. S., Dicker, S. R., Korngut, P. M., et al. 2010, *ApJ*, 716, 739
 Moravec, E., Gonzalez, A., Dicker, S., et al. 2020, *ApJ*, 898, 145
 Mroczkowski, T., Nagai, D., Basu, K., et al. 2019, *SSRv*, 215, 17
 Planck Collaboration, Ade, P. A. R., Aghanim, N., et al. 2015, *A&A*, 581, A14
 Rettura, A., Chary, R., Krick, J., & Etori, S. 2018, *ApJ*, 867, 12
 Robitaille, T., & Bressert, E. 2012, APLpy: Astronomical Plotting Library in Python, v2.0., Astrophysics Source Code Library, ascl:1208.017
 Romero, C. E., Mason, B. S., Sayers, J., et al. 2015, *ApJ*, 807, 121
 Romero, C. E., Sievers, J., Ghirardini, V., et al. 2020, *ApJ*, 891, 90
 Ruppin, F., McDonald, M., Brodwin, M., et al. 2020, *ApJ*, 893, 74
 Rykoff, E. S., Koester, B. P., Rozo, E., et al. 2012, *ApJ*, 746, 178
 Saro, A., Bocquet, S., Rozo, E., et al. 2015, *MNRAS*, 454, 2305
 Simet, M., McClintock, T., Mandelbaum, R., et al. 2017, *MNRAS*, 466, 3103
 Wik, D. R., Sarazin, C. L., Ricker, P. M., & Randall, S. W. 2008, *ApJ*, 680, 17
 Williamson, R., Benson, B. A., High, F. W., et al. 2011, *ApJ*, 738, 139
 Wright, E. L., Eisenhardt, P. R. M., Mainzer, A. K., et al. 2010, *AJ*, 140, 1868
 Wylezalek, D., Vernet, J., De Bruck, C., et al. 2014, *ApJ*, 786, 17
 Young, A. H., Mroczkowski, T., Romero, C., et al. 2015, *ApJ*, 809, 185